IEEE Photonics Journal
An IEEE Photonics Society Publication

Open Access

Ultra-Broadband, Fabrication Tolerant Optical Coupler for Arbitrary Splitting Ratio Using Particle Swarm Optimization Algorithm

Volume 12, Number 5, October 2020

Lemeng Leng
Minfeng Jin
Zhongzhi Lin
Chenbin Zhang
Ding Ding
Wei Jiang

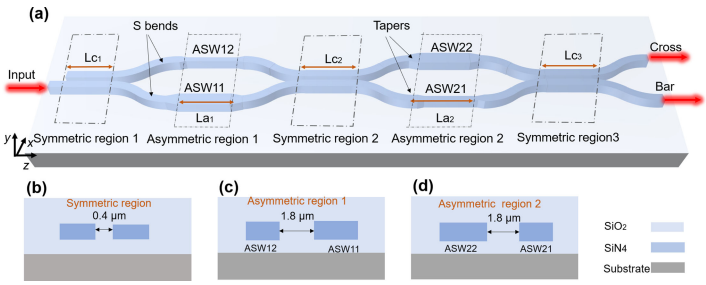

DOI: 10.1109/JPHOT.2020.3029059

Ultra-Broadband, Fabrication Tolerant Optical Coupler for Arbitrary Splitting Ratio Using Particle Swarm Optimization Algorithm

Lemeng Leng, Minfeng Jin, Zhongzhi Lin, Chenbin Zhang, Ding Ding, and Wei Jiang

College of Engineering and Applied Sciences, Key Laboratory of Intelligent Optical Sensing and Manipulation (Nanjing University), Ministry of Education, and National Laboratory of Solid State Microstructures, Nanjing University, Nanjing 210093, China

DOI:10.1109/JPHOT.2020.3029059

Manuscript received August 7, 2020; revised September 14, 2020; accepted October 1, 2020. Date of publication October 7, 2020; date of current version October 16, 2020. This work was supported in part by the Natural Science Foundation of China under Grant 61775094, in part by the Fundamental Research Funds for the Central Universities under Grant 021014380142, and in part by Jiangsu Innovative/Entrepreneurial Teams and the National Key R&D Program of China under Grants 2017YFA0303700 and 2017YFA0303704. Corresponding author: Wei Jiang (e-mail: weijiang@nju.edu.cn.)

Abstract: This work presents a design approach of multi-segment directional couplers with ultra-broadband flat spectra and benign fabrication tolerance on the silicon nitride platform. Using particle swarm optimization, we optimize design parameters of multiple coupling regions and asymmetric decoupling regions in the multi-segment couplers, and synthesize optimized structures for the intended power splitting ratio over optical telecommunication O, S, E, and C bands. To efficiently model the device with many structural parameters, each part of the fundamental structure is separately modelled by the most efficient method, including effective index method, coupled mode theory, and transfer matrix method to construct the high-dimensional design space. By choosing a proper evaluation function, the optimized couplers achieve flat spectra with less than $\pm$2% fluctuation over $\sim$300 nm spectrum for 50%/50%,30%/70% and 10%/90% splitting ratios, which is well verified by 3D FDTD. We also discuss performance degradation caused by fabrication variations and offer a general strategy to enhance fabrication tolerance for the broadband optical couplers with asymmetric decoupling regions.

Index Terms: Broadband, Silicon nitride, Power splitter, Directional couplers.

1. Introduction

Directional couplers (DCs) are fundamental building blocks for power distribution in photonic integrated circuits for many applications including on-chip photonic applications, such as optical switches and reconfigurable wavelength division multiplexing (WDM) photonic networks [1]–[4], modulators [5], optical phased arrays [6], [7], all-optical neutral networks [8] and quantum photonic systems [9]. An ideal power distribution component should exhibit wide bandwidth, low intrinsic excess loss, high fabrication tolerance, arbitrary splitting ratios with small deviation, easily fabricated, and ability to handle high power optical signal. Multimode interferences are popular options for power splitting, but are difficult to realize broad band operation with low loss and arbitrary

splitting ratio due to self-imaging limitations [10]. Insertion loss are theoretically relatively low for regular DCs based on two parallel straight waveguides, but the power splitting ratio of such devices are sensitive to operational wavelength due to wavelength-dependent coupling, which limits DC performance for photonic integrated circuits. Several approaches to extending bandwidth for coupling structures have been proposed, including multi-segments DCs [11]–[14], asymmetric DCs (ADCs) [15], [16], adiabatic DCs [17] and subwavelength gratings.

DCs in [Ref. [11], [12], [15]–[17] can realize relatively broadband operations for arbitrary power splitting ratio by compensating the coupling power ratio and phase delay between the two propagation paths in the waveguides system. For example, the multi-segment DCs demonstrated in Ref [12]. introduces asymmetric waveguides between two uniform DCs to simplify the optimizing space, the power variations are up to $\pm$3.5% over a 100 nm bandwidth in theory. [Ref. [16] proposes a design concept utilizing genetic algorithm (GA) to optimizing gap, widths combination of the segmented coupling waveguides, which can achieve 100 nm bandwidth for arbitrary splitting ratio with $\pm$2% power variation. However, the operation bandwidths of such DCs mentioned above are difficult to be extended further. Aside from traditional waveguide-based devices, sub-wavelength gratings assisted DCs (SWG-DCs) can achieve ultra-broadband operations [18]–[21]. For example, as shown by the simulation results in [Ref. [21], the SWG-DC achieves $\sim$140 nm bandwidth for design-Intended power splitting ratio with a maximum power deviation of $\sim\pm$6%.

Furthermore, ability to handle high power distribution is another demand of broadband DCs for the applications such as multi-channel WDM [2] and Lidar [7]. However, two-photon absorption (TPA) and four-wave mixing will lead to additional loss and wavelength conversion for high power propagation in silicon waveguides. Silicon nitride can minimize these issues and better handle high optical power [22], [23].

By considering the operation bandwidth, power deviation, robustness against to the fabrication variation, ability to handle high power transmission and latitude of choosing splitting ratios, this paper proposes a design approach based on multi-segment couplers built on a silicon nitride platform. The fundamental structure here comprises three symmetric coupling segments with different coupling ratios for power exchange and dual internally stretched asymmetric segments with different length for decoupling and balanced phase compensation. Focus on ultra-broadband operations, our design approach optimizes all design parameters of all segments rather than only optimizing the phase delay segments between three identical couplers (e.g., [Ref. [14]). By considering all parameters of all segments, we can explore significantly higher dimensional design-space and offer an ultra-broad bandwidth beyond the 2D design space offered by optimizing the two phase delay segments. To effectively search through the large design space characterized by complex nonlinear dependence of the evaluation function for ultra-broadband flat spectrum, we utilize the particle swarm optimization (PSO) algorithm with properly constructed evaluation function. The optimized 50%/50%,30%/70% and 10%/90% DCs can theoretically realize intended power splitting ratios with low power variations ($<\pm$2%) over $\sim$300 nm bandwidth. We also discuss the reason of broadband performance degradation caused by fabrication variations and propose a general optimal strategy to enhance tolerance to fabrication variations for such devices.

2. Design and Analysis

2.1 Device Schematic

Fig. 1 shows the fundamental structure and representative segment cross-sections. We design the devices on a 400 nm silicon nitride layer deposited on a silicon wafer with sufficiently thick oxide layer, and employed a 2 μm silicon oxide cladding layer over the device. Fig. 1(b) shows two parallel strip 1 μm waveguides form symmetric regions with 400 nm gap. The relatively small silicon nitride refractive index compared with silicon make it difficult to realize an effective index difference between odd and even modes using different waveguides widths, which is required to compensate for phase differences and obtain stable splitting ratios over a broad wavelength range.

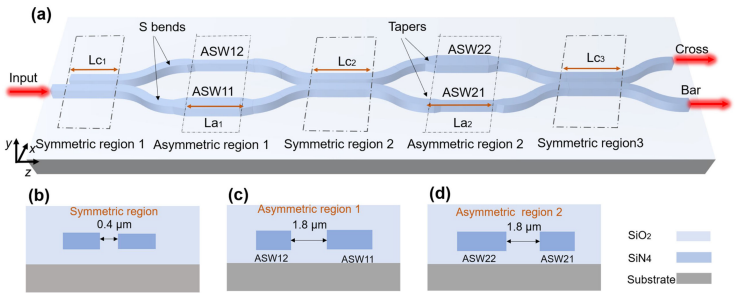

Fig. 1. Structure of the proposed multi-segment directional coupler. (a) Schematic. (b) Cross section of the symmetric regions. (c) Cross section of the asymmetric region 1. (d) Cross section of the asymmetric region 2.

Hence, we stretch the parallel strip waveguides with 1.8 μm gap to decouple between the two arms, employing asymmetric waveguides with 1 μm linear tapers, providing phase control and decoupled propagation. Fig. 1(c) shows waveguides 1 and 2 widths $=$ 1.2 and 0.8 μm, respectively, in asymmetric region 1, and Fig. 1(d) shows that this width combination is exchanged for asymmetric region 2. Mirrored S bends with a lateral offset of 0.75 μm and a length of 15 μm is employed to stretch the coupling waveguides and produce the 1.8 μm gap. Difference of the phase control segments are designed to balance the loss between the two paths, which introduced by the tapers. Output characteristics based on this pre-optimized structure is determined by parameters Lc_1, La_1, Lc_2, La_2 and Lc_3 as shown in Fig. 1. Note that there may exist two perspectives on such a structure. One considers it as two cascaded Mach-Zehnder interferometers and the other considers it as a normal directional coupler with certain segments (La_1 and La_2) decoupled through internal stretching. The first perspective usually assumes the three couplers (Lc_1, Lc_2 and Lc_3) have fixed coupling ratios and the broadband behavior is solely controlled by two phase segments, which limits the design space to 2D. The second perspective is more general and recognizes that both the phase shift and coupling ratios between the two paths can be varied to more effectively reach the broadband goal. Large internal stretching allows for pure phase control in La_1 and La_2, which may be conducive for simplified control. At what points we should switch from phase control to coupling ratio control is also important. Powered by the PSO algorithm, we are able to search the high-dimensional design space of multi-segments DCs shown in Fig. 1 to reach our goal.

2.2 Analysis

Many numerical methods have been employed to model optical device output characteristics, such as FDTD, beam propagation method and finite element methods. However, these methods generally require considerable computing resources for only a single device structure. Meanwhile heuristic algorithms, such as particle swarm PSO [24] and GA [16], are suitable to search for optimal design parameters for optical devices with multiple variables, these iteration approaches must perform numerical simulations many times. Thus, it is difficult to obtain an optimum solution in reasonable time using 3D FDTD. Therefore, we divide the device into multiple parts and combine effective index method (EIM), coupled mode theory (CMT), and transfer matrix method (TMM) to calculate the overall output spectra efficiently. Based on such efficient calculation, we can obtain a mapping between the structural parameters and the output spectra, which forms the high-dimensional design space. Subsequently, the PSO optimization can search efficiently in such a design space to realize good performance in across a broad band.

The proposed structure shown in Fig. 1 can be divided into a series of cascaded matrixes, and hence output characteristics can be expressed as

$$\begin{bmatrix} E_{bar} \\ E_{cross} \end{bmatrix} = S_s \cdot C_3 \cdot S_c \cdot T_2 \cdot A_2 \cdot T_2 \cdot S_s \cdot C_2 \cdot S_c \cdot T_1 \cdot A_1 \cdot T_1 \cdot S_s \cdot C_1 \cdot \begin{bmatrix} E_{in} \\ 0 \end{bmatrix} \quad (1)$$

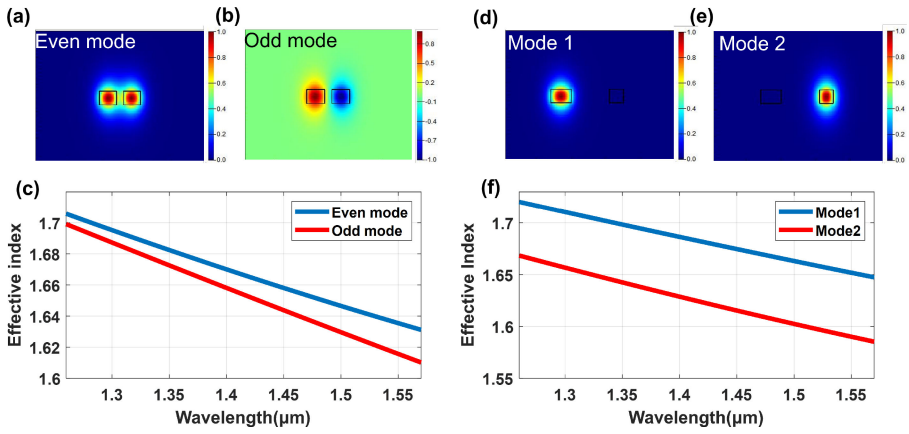

Fig. 2. (a) even and (b) odd mode profiles of the coupled waveguides and corresponding (c) effective indices of the symmetric regions. Guided mode profiles for (d) 1.2 μm and (e) 0.8 μm waveguides; and corresponding (f) effective indices of the asymmetric waveguides.

where E_{bar} and$E_{cross}$are the bar and cross output electric field, respectively; E_{in} is the input electric field; Ci is the transfer matrix for the *i*-th coupling region; S_s and S_c are transfer matrices for the paired separating and converging waveguides, respectively; A_1 and A_2 are propagating characteristics for asymmetric regions 1 and 2, respectively; T_1 and T_2 are propagation matrices for the linear tapers between S bends and asymmetric regions. From CMT, the parallel and equal width waveguide coupling matrix for coupling region *j* can be expressed as [25]

$$C_j(\lambda) = \begin{bmatrix} t(\lambda) & -jk(\lambda) \\ -jk(\lambda) & t(\lambda) \end{bmatrix} \cdot e^{-j\phi(\lambda)} \tag{2}$$

where$\lambda$is the input wavelength; *t*is the transition coefficient.

$$t(\lambda) = \cos\left(\frac{Lc_i\pi}{\lambda}(n_e(\lambda) - n_o(\lambda))\right) \tag{3}$$

*k*is the coupling coefficient,

$$k(\lambda) = \sin\left(\frac{Lc_i\pi}{\lambda}(n_e(\lambda) - n_o(\lambda))\right) \tag{4}$$

ϕ is an overall phase shift term in Eq. (2) arising from the coupling region,

$$\phi(\lambda) = \frac{Lc_i\pi}{\lambda}(n_e(\lambda) + n_o(\lambda)) \tag{5}$$

Lc_i is the coupling length for the *i*-th ($i = 1, 2, 3$) coupling region; and $n_e(\lambda)$ and $n_o(\lambda)$ are effective indices for even and odd modes in the coupled waveguides system with major component E_x for transverse electromagnetic polarization.

Fig. 2 shows $n_e(\lambda)$ and $n_o(\lambda)$ in the weak coupling limit, calculated using the eigenmode solver. Material dispersions of the silicon nitride and silicon oxide were derived from [Ref. [26] and [Ref. [27]. We omitted waveguide losses for this case because silicon nitride waveguide loss is significantly less than for silicon waveguides [22].

Propagation matrices for asymmetric regions 1 and 2 phase control sections can be expressed as

$$A_1(\lambda) = \begin{bmatrix} \exp(-j\frac{2\pi n_{W1}(\lambda)}{\lambda}La_1) & 0 \\ 0 & \exp(-j\frac{2\pi n_{W2}(\lambda)}{\lambda}La_1) \end{bmatrix} \tag{6}$$

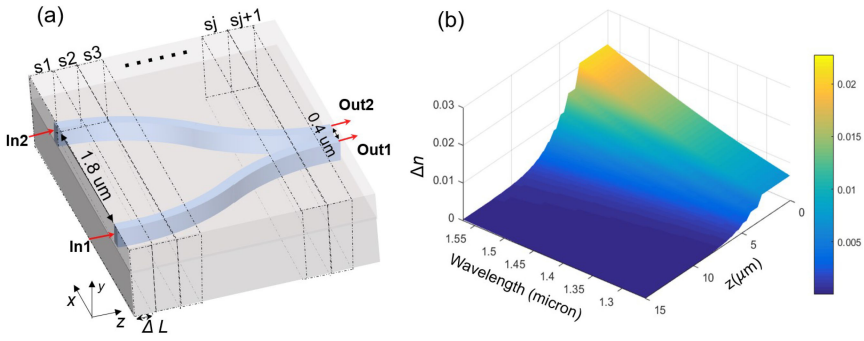

Fig. 3. (a) Perspective view for discretized converging S bend with divisions indicated by the dashed boxes. Adjacent waveguide gaps = 1.8 and 0.4 μm at incident and terminal interfaces, respectively. (b) Effective indices difference Δn calculate along z axis propagation direction.

and

$$A_2(\lambda) = \begin{bmatrix} \exp(-j\frac{2\pi n_{W2}(\lambda)}{\lambda} La_2) & 0 \\ 0 & \exp(-j\frac{2\pi n_{W1}(\lambda)}{\lambda} La_2) \end{bmatrix} \tag{7}$$

respectively, where La_1 and La_2 are propagation lengths for region 1 and 2; and $n_{W1}(\lambda)$ and $n_{W2}(\lambda)$ are effective indices for decoupled modes localized in waveguides 1 and 2, as shown in Fig. 2(f), with field profiles as shown in Figs. 2(d) and (e).respectively.

Propagating matrixes for the 1 μm linear tapers can be expressed as

$$T_1 = \begin{bmatrix} \exp(-j\varphi_1(\lambda)) & 0 \\ 0 & \exp(-j\varphi_2(\lambda)) \end{bmatrix} \tag{8}$$

and

$$T_2 = \begin{bmatrix} \exp(-j\varphi_2(\lambda)) & 0 \\ 0 & \exp(-j\varphi_1(\lambda)) \end{bmatrix} \tag{9}$$

where $\varphi_1(\lambda)$ and $\varphi_2(\lambda)$ are phase delay introduced by the 1-1.2 μm and 1-0.8 μm tapers, respectively. Here, we extracted $\varphi_1(\lambda)$ and $\varphi_2(\lambda)$ using 3D FDTD.

In Eq. (1), S_c and $S_s$are the transmission matrixes of the S bends for waveguides converging and separating. Omitting the coupling effect in network analyses has negative effect on optimization. Therefore, we discretized the structure into a series of cascaded slices along the propagation directions to obtain coupling and propagation behavior in the S bends, for uniform length ΔL= 50 nm as shown in Fig. 3(a). Gaps between adjacent waveguides for each slice are functions of propagation length, where the effective difference between even mode and odd mode indices for the i-th slice is $\Delta n^i(\lambda) = n_e^i(\lambda) - n_o^i(\lambda))$, as shown in Fig. 3(b), calculated by the eigenmode solver. From CMT for a symmetric coupling system,

$$S_c = \prod_{i=N}^{i=1} \begin{bmatrix} \cos(\frac{\Delta L\pi}{\lambda}\Delta n^i(\lambda)) & -j\sin(\frac{\Delta L\pi}{\lambda}\Delta n^i(\lambda)) \\ -j\sin(\frac{\Delta L\pi}{\lambda}\Delta n^i(\lambda)) & \cos(\frac{\Delta L\pi}{\lambda}\Delta n^i(\lambda)) \end{bmatrix} \cdot \exp\left(-j\frac{\Delta L\pi\,(n_e^i(\lambda) + n_e^i(\lambda))}{\lambda}\right) \tag{10}$$

and

$$S_s = \prod_{i=1}^{i=N} \begin{bmatrix} \cos(\frac{\Delta L\pi}{\lambda}\Delta n^i(\lambda)) & -j\sin(\frac{\Delta L\pi}{\lambda}\Delta n^i(\lambda)) \\ -j\sin(\frac{\Delta L\pi}{\lambda}\Delta n^i(\lambda)) & \cos(\frac{\Delta L\pi}{\lambda}\Delta n^i(\lambda)) \end{bmatrix} \cdot \exp(-j\frac{\Delta L\pi\,(n_e^i(\lambda) + n_e^i(\lambda))}{\lambda}) \tag{11}$$

where N is the total number of divided slices in the paired S bends. Difference between S_c and S_s in Eqs. (10) and (11) depends on the propagation direction. The S bend for separating waveguides can be treated as a back-propagation situation relative to the converging S bends shown in Fig. 3(a).

3. Particle Swarm Optimization and Simulation

3.1 Analysis

The wavelength-dependent power splitting ratio can be easily calculated from the analysis using TMM, which gives a mapping between the structural parameters and the output spectra and effectively spans the high-dimensional design space. To perform PSO in such a design space, we first define figure-of-merit (FOM) as an evaluation parameter (or evaluation function), *EP*, to evaluate broadband characteristics for arbitrary power splitting ratios within the desired wavelength range. For our case, we set 45 frequency points from 1260 to 1560 nm and define evaluation parameter as

$$EP = \frac{1}{\sum_{i=1}^{45} \left(\left| \eta_{cross}(\lambda_i) - Tr \right| + \left| \eta_{bar}(\lambda_i) - (1 - Tr) \right| \right)} \tag{12}$$

where Tr is the target power splitting ratio for the cross port within the wavelength range to be optimized. For example, consider 3 dB broadband splitter with $Tr = 50\%$. Then η_{bar} and $\eta_{cross}$are normalized power splitting ratios for the bar and cross ports wavelength λ_i, which defined as

$$\eta_{bar} = \frac{|E_{bar}|^2}{|E_{bar}|^2 + |E_{cross}|^2}, \ \eta_{corss} = \frac{|E_{cross}|^2}{|E_{bar}|^2 + |E_{cross}|^2} \tag{13}$$

By introducing such an evaluation parameter, we can then transfer optimizing multiple uncertain variants into maximizing *EP* for the selected *Tr*. In the PSO optimization, a DC structure with a specific combination of parameters is represented by a "particle". To start optimizing, we initialized particles x and velocity vectors v, where x elements correspond to [Lc_1, La_1, Lc_2, La_2, Lc_3] and v is a measure of the change of x after an iteration. We denote the k-th (k = 1, 2, …, 200) particle and velocity vector in the l-th (l = 1, 2, …, 200) iteration as

$$x_k^l = [x_1, x_2, x_3, x_4, x_5], \quad v_k^l = [v_1, v_2, v_3, v_4, v_5] \tag{14}$$

Before the algorithm begins, the particles in the swarm are random values [0,50] μm with corresponding random velocities $[-25, 25]$ μm. We then calculate spectral output with each particle and hence *EP* for these initial values and find the individual best P^l and global best Pg^l in this iteration according to *EP*. For k-th particle the individual best P_k^l is the best parameter combination for this particle from the first to l-th iteration. The historical global best $Pg^l$is the best parameter combination of all particles. For l+1 iteration, all particles and corresponding velocity vectors are updated according as [28]

$$\begin{aligned} v_k^{l+1} &= \omega \cdot v_k^l + c_1 \cdot (P_k^l - x_k^l) + c_2 \cdot (Pg^l - x_k^l) \\ x_k^{l+1} &= x_k^l + v_k^l \end{aligned} \tag{15}$$

where $\omega = 0.8$, and c1 = c2 = 1 constants are common values for inertia, individual learning, and swarm learning factors, respectively. After the $l + 1$ iteration, Pg^l is updated if *EP* for any particle $x_k^{l+1} >$ historical best *EP*, but if the new best *EP* $<$ historical best *EP* calculated for Pg^l, then $Pg^{l+1} = Pg^l$. For the k-th particle, the individual best P_k^{l+1} updates when new calculated *EP* $>$ historical best *EP* in all previous iterations. Optimization is terminated when *EP* remains almost constant within convergence tolerance = 0.001 after 150 iterations and global best *EP* > 2. Finally, based on the model analysis, we build the optical transform model and develop our own code for the PSO algorithm.

Fig. 4 shows optimization iteration process and intermediate results for 3 dB power splitting using 200 particles, where the red solid line indicates maximum particle *EP* in each iteration. Maximum *EP* increased from 0.2134 to 1.097 by iteration 40. Fig. 4(b)–(d) shows normalized power splitting ratios for the best performance particles from iteration 1,20 and 40 in wavelength range 1260–1570 nm, respectively. Although *EP* is not ideal compared to the global best solution, maximum power splitting deviation is already small enough at 48.2%/51.8% after 40-th iteration. Best *EP* then increased rapidly from 1.097 to 1.714 after two further iterations, accompanied with

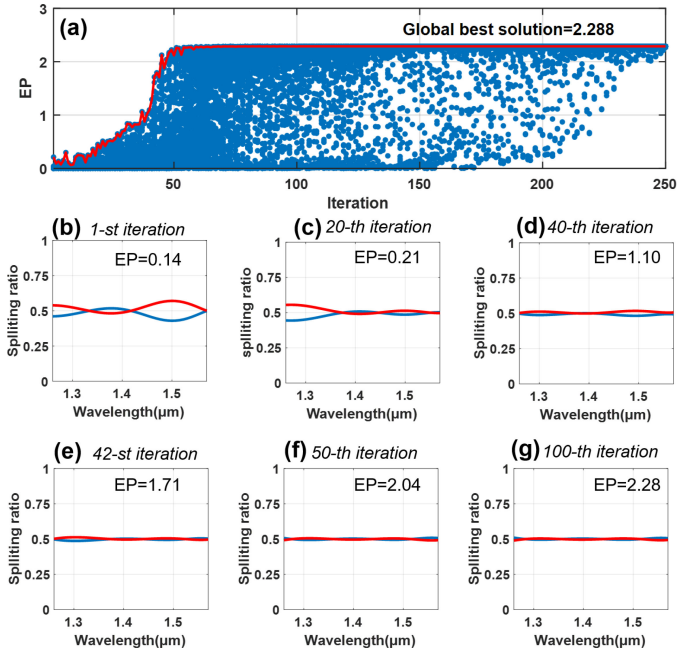

Fig. 4. Iteration process and intermediate results. (a) Particle evaluation parameter (EP) evolution for 3 dB broadband power splitter; scattered blue points are calculated EP for of all particles during optimization, and solid red line indicates best performance in every iteration. Normalized power splitting ratio spectra obtained from best parameter combination after (b) 1, (c) 20, (d) 40, (e) 42, (f) 50, and (g) 100 iterations in the target wavelength range 1260–1570 nm.

TABLE 1
Design Parameters of Optimized Broadband DCs

Designed couplers	Lc_1	La_1	Lc_2	La_2	Lc_3
10%/90%	14.1 μm	13.79 μm	34.25 μm	27.37 μm	46.29 μm
30%/70%	47.2 μm	7.5 μm	40.7 μm	27.8 μm	24.35 μm
50%/50%	38.65 μm	16.5 μm	38.86 μm	14.8 μm	44.6 μm

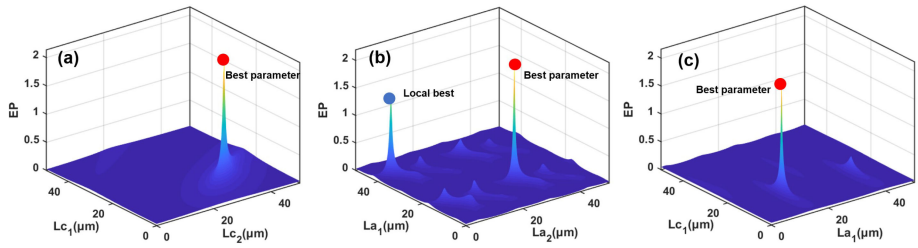

Fig. 5. Design space for optimization with respect to (a) Lc_1 and Lc_2, (b) La_1 and La_2, and (c) Lc_1 and La_1 from 0-50 μm.

reduced maximum deviation 48.7%/51.3% (Fig. 4(e)), with most particles converging to maximum 2.288 after 50 iterations. Comparing maximum *EP* between iteration 50 and 100 (Figs. 4(d) and (f), respectively) shows that broadband performance was not significantly enhanced once *EP* exceeded a particular threshold. Table 1 shows optimal design parameters and performance. Evidently, ultra-flat spectra are achieved over 1260–1570 nm in Fig. 4(g), indicating precise power splitting over an ultra-broad bandwidth.

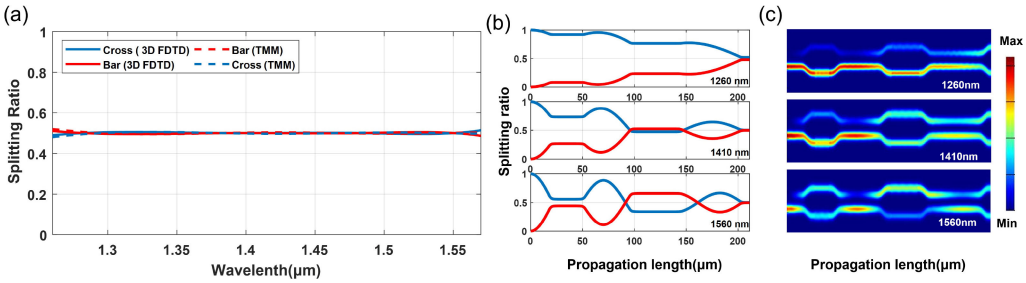

Fig. 6. 50%/50% multi-segment DC. (a) Splitting ratio of the optimized structure calculated by TMM and FDTD. (b) Power transmission of the upper path and lower path along the propagation direction calculated by TMM (the blue line: lower path, the red line: upper path) and (c) power field distributions calculated by 3D FDTD.

Fig. 5 shows the typical 3D contour maps, to help solve for the space presenting *EP* changing with respect to asymmetric region lengths, Lc_1 and Lc_2, asymmetric region lengths, La_1 and La_1, and mixed asymmetric and symmetric region lengths, La_1 and Lc_1, respectively. The sharp peaks in design space indicate that lengths of all segments contribute to the broadband and flat spectra. In Fig. 5 (b), besides the best parameter combination, $La_2 = 27.37$ μm, $La_1 = 13.8$ μm, another local best at $La_2 = 7.9$ μm, $La_1 = 42.7$ μm exists which indicates that our optimizing algorithm has found the best parameter combination in the entire design space rather than a local best.

3.2 Simulation

To verify the design approach, we simulate the optimized 50%50% DC using 3D FDTD. For comparison, Fig. 6(a) shows the normalized cross and bar ports power splitting ratios calculated by the TMM method, which shows good agreement with the FDTD method with $\pm$2% power variation within 1260–1570 nm. To further verify the accuracy of our approach, we calculate the propagation behaviors of the upper path and lower path at 1260 nm, 1410 nm and 1560 nm in Fig. 6(b), which also shows good agreement with the simulation result in Fig. 6 (c). It is easy to see that before the third coupling region, transmitted power in the upper path and lower path change frequently over the whole propagation length and optical power in the asymmetric region 2 shows visibly distinct features at these 3 wavelengths. At 1560 nm, more power is routed to the upper path; at 1410 nm, the upper and lower paths have roughly balanced power; and at 1260 nm, most power is routed to the lower path. Finally, the power at these wavelengths in each path converged to the target splitting ratio at the output ports. Note that the fanout waveguides for output can introduce a very small fraction of mode conversion ($<$0.5% in power) during the fanout process, which has negligible influence on the performance of the device. Changing the output waveguide length has virtually no effect on the device performance.

To show the ability for arbitrary splitting ratio, we optimize 30%/70% and 10%/90% DCs by changing $Tr = 0.3$ and $Tr = 0.1$ in Eq. (12), respectively. The design parameters and bandwidth calculated by TMM and FDTD are summarized in Table 1. Maximum power deviation between theorical and simulation results for 30%/70% coupler is less than 2%, and FDTD simulated $\pm$2% bandwidth over 1275–1570 nm, in reasonable agreement with the TMM calculation. Similarly, maximum power deviation for 10%/90% coupler $<$1.5% and $\pm$2% bandwidth covers the spectral range from 1260–1570 nm. Different from the 50%/50% coupler in Fig. 6, the 30%/70% coupler in Fig. 7 shows relatively small change of power re-routing over the upper and lower paths in the asymmetric region 2. Most power stays in the lower path. The 10%/90% coupler in Fig. 8 has a balanced power in the upper and lower paths in both asymmetric regions at 1260 nm; whereas at two other wavelengths, the power distributions stay in the one same path. Additionally, the power exchanging of the 30%/70% and 10%/90% couplers in Fig. 7(b) and Fig. 8(b) are dramatic between the upper and lower path which will produce slightly larger deviations in spectrum than 50%/50%

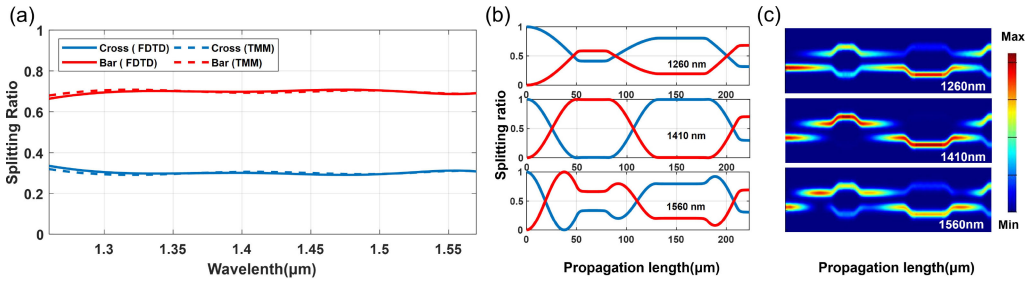

Fig. 7. 30%/70% multi-segment DC. (a) Splitting ratio of the optimized structure calculated by TMM and FDTD. (b) Power transmission of the upper path and lower path along the propagation direction calculated by TMM (the blue line: lower path, the red line: upper path) and (c) power field distributions calculated by 3D FDTD.

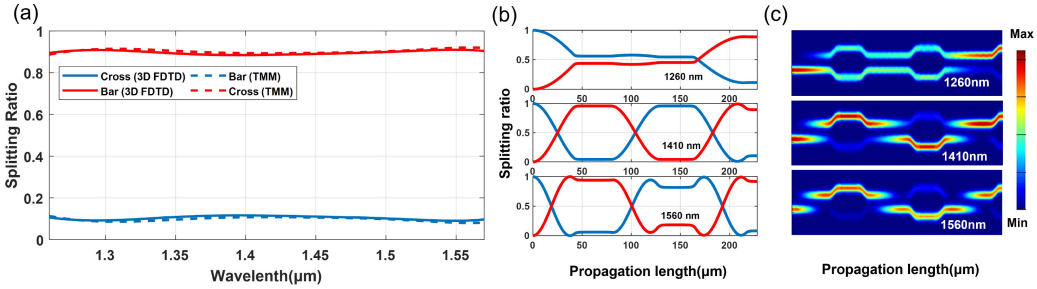

Fig. 8. 10%/90% multi-segment DC. (a) Splitting ratio of the optimized structure calculated by TMM and FDTD. (b) Power transmission of the upper path and lower path along the propagation direction calculated by TMM (the blue line: lower path, the red line: upper path) and (c) power field distributions calculated by 3D FDTD.

TABLE 2
Comparison of Arbitrary DCs in the Literature With Simulation Results

Ref	type	Simulated Bandwidth	Simulated Power deviation	Simulated Insertion loss
[12]	Multi segment DC	~100nm	±3.5%	N/A
[16]	Asymmetric DC	~100nm	±2%	0.013dB
[17]	Adiabatic coupler	~100nm	±1%	N/A
[21]	SWGDC	~100nm	±6%	0.96dB
This work	Multi segment DC	~300nm	±2%	0.023dB

coupler. These diverse behaviors are also indicative of the complex phase-compensation needed to achieve stable power splitting over an ultra-wide bandwidth. Table 2 provides a comparison of this work with some arbitrary DCs designed on the comparable mode in previous literature. Note that as the materials (and the index contrast) used in these studies are very different, the dimensions of these devices differ widely. For example, the bending radius allowed for silicon waveguides in some studies is widely different from that of silicon nitride waveguides. Hence the device dimensions are largely influenced by material choice (especially index contrast) and do not reveal intrinsic properties of the device design, which is the focus of this work. Hence the device dimensions are not included in comparison.

4. Fabrication Tolerance

Over an ultra-broad bandwidth, fabrication variation can possibly induce more performance variation than a relatively narrow bandwidth. Therefore, we investigated fabrication tolerance of the

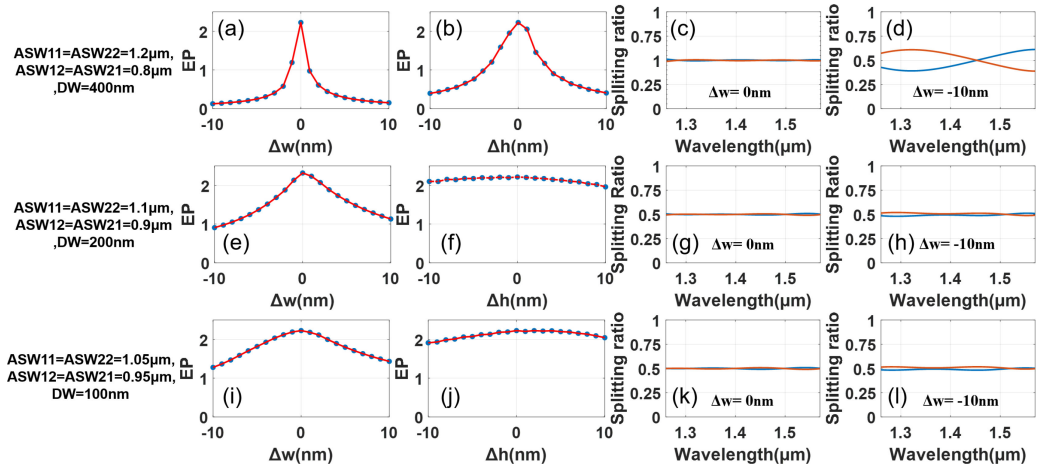

Fig. 9. Fabrication tolerance analysis using the evaluation parameter (*EP*) with respect to Δw for (a) DW $= 400$ nm, (e) DW $= 200$ nm, and (i) DW $= 100$ nm. *EP* with respect to Δh for (b) DW $= 400$ nm, (f) DW $= 200$ nm and (j) DW $= 100$ nm. Splitting ratios for (c) $\Delta w = 0$ and (d) $\Delta w = -10$ nm in (a); (g) $\Delta w = 0$ and (h) $\Delta w = -10$ nm in (e); and (k) $\Delta w = 0$ and (l) $\Delta w = -10$ nm in (i).

proposed design, considering effects from total waveguides widths (Δw) and thickness (Δh) variations with a constant center-to-center distance that could possibly occur during lithography and etching [29], which automatically takes into consideration the gap variation in the coupling regions. To intuitive represent the degradation caused by the fabrication variations, we use single parameter, *EP*, defined in Eq. (11) to evaluate robustness of our design. Fig. 9 shows fabrication tolerances for the optimized 50%/50% broad band DCs with different waveguide width combinations (DW) in the asymmetric regions1 and asymmetric regions2 as total waveguide widths (Δw) and thickness (Δh) changes from -10 nm to 10 nm. Fig. 9 (a) and (b) show the EP with various Δw and Δh, respectively, for asymmetric region waveguide widths ASW11 $=$ ASW22 $=$ 1200 nm and ASW12 $=$ ASW21 $=$ 800 nm. It suggests that the broadband performance is sensitive to the fabrication variations and the Δw has a more negative impact thanΔh. Then, we update the structures with different DW and optimize 50%/50% power splitting ratio with PSO. To ensure a fair comparison, global best *EP* is optimized around 2.2.

Fig. 9(e), (f), (i) and (j) show the calculated EP for DW $=$ 200 and 100 nm as functions of Δw and Δh. As the devices are less sensitive toΔh, we focus on the fabrication variation of Δw. Splitting ratios of the devices optimized using different DW are shown in Fig. 9 (c), (d), (g), (h), (k) and (l) when there is a fabrication variation of $\Delta w=$ 10 nm and $\Delta w=$ 0 nm. In Fig. 9(c) and (d) the maximum power variation degenerated sharply from %2 to 16% as Δwchanges from 0 nm to -10 nm. For the device with DW $=$ 200 nm, even EP is reduced from 2.309 to 0.978, the maximum variations remained within an acceptable range of $-2\% \sim 1.2\%$. For the device optimized with DW $=$ 100 nm, as E is reduced from 2.22 to 1.278 when $\Delta w= -10$ nm, the power variation only increases from $-0.7\sim0.9\%$ to $-1.3\% \sim 1\%$. Evidently, the $\pm2\%$ bandwidth of this device under fabrication variation with DW less than 200 nm can still maintain 310 nm.

By comparing with Fig. 9 (a),(b), (e), (f), (i), and (j),it is interesting to note that broadband performance of such multi-segment DCs has become less sensitive to Δw and Δh as the DW reduced from 400 nm to 100 nm. This can be explained by that the degenerated broadband performance is largely affected by the phase mismatch from the large width difference DW between the asymmetric waveguides, which disrupting power and phase compensation in this complex system. If asymmetry (i.e., DW) between the two waveguides becomes fairly small, the two branches are approaching a balanced configuration, which tends to be less sensitive to fabrication variation. Meanwhile, the broadband performance of the devices is tolerant to the variation of splitting ratios of the DCs in the symmetric regions. Based on the above analysis, we can design and optimize fabrication tolerant

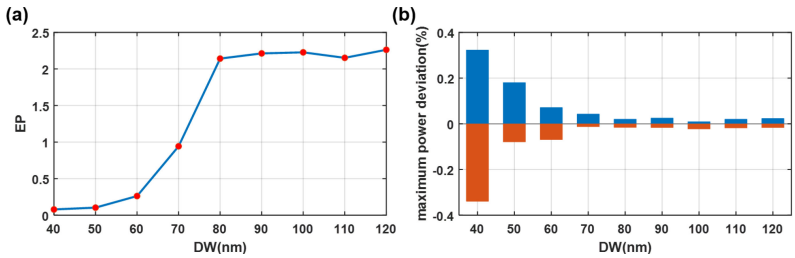

Fig. 10. (a) Best evaluation parameter (*EP*) and (b) maximum bar port power deviations with respect to DW.

multi-segment DCs by introducing asymmetric waveguides with smaller DW in the fundamental structure, which can be fabricated easily with good process controllability and high yield.

The method to enhance fabrication tolerance can be extended to other broadband DCs employing asymmetric waveguides. However, although the decreased DW can enhance fabrication tolerance for the proposed design, it also affects optimization for broadband performance. Fig. 10(a) shows best *EP* optimized by PSO with respect to DW and Fig. 10(b) shows the corresponding maximum power variation with respect to DW for the best solutions. The algorithm can always find optimal combinations to achieve 310 nm bandwidth if DW $>$80 nm, with maximum power deviation $<\pm$2%. However, when DW$<$ 80 nm, asymmetric waveguides cannot provide sufficient phase offset within the searching range 0-50 μm. Although suitable combinations providing good broadband performance can be obtained for DW $<$ 80 nm by expanding the search space, this will increase overall device size.

5. Conclusion

This work proposes a design approach of multi-segments DCs for arbitrary power splitting on the silicon nitride platform. Design parameters of each coupling region and phase control region in the fundamental structure are engineered by the PSO algorithm. The PSO algorithm-optimized 10%/90%, 30%70% and 50%50% multi-segment DCs achieve excellent broadband performance with ultra-flat spectra with $<\pm$2% fluctuation over $\sim$300 nm bandwidth. To perform the PSO efficiently, the design space is constructed by combining EIM, CMT, and TMM rather than time-consuming FDTD simulations. Calculated results of the optimized DCs are verified by 3D FDTD simulations. The complex propagation behaviors in two paths over an ultra-wide bandwidth have shown that the PSO algorithm combined with a proper evaluation function is effective in searching for a non-trivial broadband behavior in a complex high-dimensional design space. In addition, we explore the broadband performance degeneration which is caused by fabrication variations in such devices and shown the method to enhance fabrication tolerance by using smaller width differences between the asymmetric waveguides. Moreover, Bandwidth of such multi-segments DCs can be further expand to L band by cascading one or more phase control and coupling segments powered by the PSO algorithm. In summary, the multi-segment DCs optimized with the proposed approach can achieve excellent performance, fabrication tolerance and offer good candidates for applications requiring ultra-broadband power distribution. Note that our approach is a general design approach for broadband power splitting applicable to other waveguide platforms (e.g., silicon or InP) as well if the weak coupling, mode localization and enough phase shift can be satisfied.

References

[1] S. Chen, Y. Shi, S. He, and D. Dai, "Low-loss and broadband 2 $\times$ 2 silicon thermo-optic Mach-Zehnder switch with bent directional couplers," *Opt. Lett.*, vol. 41, no. 4, pp. 836–839, Feb. 2016.
[2] H. Nishi *et al.*, "Integration of eight-channel directly modulated membrane-laser array and SiN AWG multiplexer on si," *J. Lightw. Technol.*, vol. 37, no. 2, pp. 266–273, Jan. 2019.

[3] H. Xu and Y. Shi, "Flat-top CWDM (de)multiplexer based on MZI with bent directional couplers," *IEEE Photon. Technol. Lett.*, vol. 30, no. 2, pp. 169–172, Jan. 2018.
[4] S. Chen, Y. Shi, S. He, and D. Dai, "Compact eight-channel thermally reconfigurable optical add/drop multiplexers on silicon," *IEEE Photon. Technol. Lett.*, vol. 28, no. 17, pp. 1874–1877, Sep. 2016.
[5] Z. Lu *et al.*, "High-performance silicon photonic tri-state switch based on balanced nested Mach-Zehnder interferometer," *Sci. Rep.*, vol. 7, 2017, Art. no. 12244.
[6] Y. Zhang *et al.*, "Sub-wavelength-pitch silicon-photonic optical phased array for large field-of-regard coherent optical beam steering," *Opt. Express*, vol. 27, no. 4, pp. 1929–1940, Feb. 2019.
[7] N. A. Tyler *et al.*, "SiN integrated optical phased arrays for two-dimensional beam steering at a single near-infrared wavelength," *Opt. Express*, vol. 27, no. 4, pp. 5851–5858, Feb. 2019.
[8] Y. Shen *et al.*, "Deep learning with coherent nanophotonic circuits," *Nature Photon.*, vol. 11, no. 7, pp. 441–446, Jun. 2017.
[9] M. Poot, C. Schuck, X.-S. Ma, X. Guo, and H. X. Tang, "Design and characterization of integrated components for SiN photonic quantum circuits," *Opt. Express*, vol. 24, no. 7, pp. 6843–6860, Mar. 2016.
[10] L. Soldano and E. Pennings, "Optical multimode interference devices based on self-imaging—Principles and applications," *J. Lightw. Technol.*, vol. 13, no. 4, pp. 615–627, Apr. 1995.
[11] S. Nevlacsil *et al.*, "Broadband SiN asymmetric directional coupler for 840 nm operation," *OSA Continuum*, vol. 1, no. 4, pp. 1324–1331, Dec. 2018.
[12] Z. Lu *et al.*, "Broadband silicon photonic directional coupler using asymmetric-waveguide based phase control," *Opt. Express*, vol. 23, no. 3, pp. 3795–3808, Feb. 2015.
[13] A. B. M. D., "Perfect optics with imperfect components," *Optica*, vol. 2, no. 8, pp. 747–750, Aug. 2015.
[14] M. Wang, A. Ribero, Y. Xing, and W. Bogaerts, "Tolerant, broadband tunable 2×2 coupler circuit," *Opt. Express*, vol. 28, no. 4, pp. 5555–5566, Feb. 2020.
[15] H. Morino, T. Maruyama, and K. Iiyama, "Reduction of wavelength dependence of coupling characteristics using si optical waveguide curved directional coupler," *J. Lightw. Technol.*, vol. 32, no. 12, pp. 2188–2192, Nov. 2014.
[16] P.-H. Fu, Y.-C. Tu, and D.-W. Huang, "Broadband optical waveguide couplers with arbitrary coupling ratios designed using a genetic algorithm," *Opt. Express*, vol. 24, no. 26, pp. 30547–30561, Dec. 2016.
[17] D. Mao *et al.*, "Adiabatic coupler with design-Intended splitting ratio," *J. Lightw. Technol.*, vol. 37, no. 24, pp. 6147–6155, Dec. 15, 2019.
[18] H. Yun, L. Chrostowski, and N. A. F. Jaeger, "Ultra-broadband 2×2 adiabatic 3 dB coupler using subwavelength-grating-assisted silicon-on-insulator strip waveguides," *Opt. Lett.*, vol. 43, no. 8, pp. 1935–1938, Apr. 2018.
[19] L. Xu *et al.*, "Compact high-performance adiabatic 3-dB coupler enabled by subwavelength grating slot in the silicon-on-insulator platform," *Opt. Express*, vol. 26, no. 23, pp. 29873–29885, Nov. 2018.
[20] C. Ye and D. Dai, "Ultra-compact broadband 2×2 3 dB power splitter using a subwavelength-grating-assisted asymmetric directional coupler," *J. Lightw. Technol.*, vol. 38, no. 8, pp. 2370–2375, Apr. 2020.
[21] Y. Wang *et al.*, "Compact broadband directional couplers using subwavelength gratings," *IEEE Photon. J.*, vol. 8, no. 3, Jun. 2016, Art. no. 7101408.
[22] S. C. Mao *et al.*, "Low propagation loss SiN optical waveguide prepared by optimal low-hydrogen module," *Opt. Express*, vol. 16, no. 25, pp. 20809–20816, 2008.
[23] W. D. Sacher, Y. Huang, G. Lo, and J. K. S. Poon, "Multilayer silicon nitride-on-silicon integrated photonic platforms and devices," *J. Lightw. Technol.*, vol. 33, no. 4, pp. 901–910, Feb. 2015.
[24] S. Abbaslou, R. Gatdula, M. Lu, A. Stein, and W. Jiang, "Ultra-short beam expander with segmented curvature control: The emergence of a semi-lens," *Opt. Lett.*, vol. 42, no. 21, pp. 4383–4386, Sep. 2017.
[25] S. L. Chuang, N. Peyghambarian, and S. Koch, "Physics of optoelectronic devices," *Phys. Today*, vol. 49, no. 7, 1996, Art. no. 62.
[26] K. Luke, Y. Okawachi, M. R. E. Lamont, A. L. Gaeta, and M. Lipson, "Broadband mid-infrared frequency comb generation in a Si3N4 microresonator," *Opt. Lett.*, vol. 40, no. 21, pp. 4823–4826, Nov. 2015.
[27] I. H. Malitson, "Interspecimen comparison of the refractive index of fused silica," *J. Opt. Soc. Am.*, vol. 55, no. 10, pp. 1205–1208, Oct. 1965.
[28] J. Robinson and Y. Rahmat-Samii, "Particle swarm optimization in electromagnetics," *IEEE Trans. Antennas Propag.*, vol. 52, no. 2, pp. 397–407, Feb. 2004.
[29] Z. Lu *et al.*, "Performance prediction for silicon photonics integrated circuits with layout-dependent correlated manufacturing variability," *Opt. Express*, vol. 25, no. 9, pp. 9712–9733, Apr. 2017.